DISCOVERY OF AN INNER DISK COMPONENT AROUND HD 141569 A[*]

MIHOKO KONISHI[1], CAROL A. GRADY[2,3], GLENN SCHNEIDER[4], HIROSHI SHIBAI[1], MICHAEL W. MCELWAIN[3], ERIKA R. NESVOLD[5], MARC J. KUCHNER[3], JOSEPH CARSON[6], JOHN. H. DEBES[7], ANDRAS GASPAR[4], THOMAS K. HENNING[8], DEAN C. HINES[7], PHILIP M. HINZ[4], HANNAH JANG-CONDELL[9], AMAYA MORO-MARTÍN[7], MARSHALL PERRIN[7], TIMOTHY J. RODIGAS[5,13], EUGENE SERABYN[10], MURRAY D. SILVERSTONE[2], CHRISTOPHER C. STARK[7], MOTOHIDE TAMURA[11], ALYCIA J. WEINBERGER[5], AND JOHN. P. WISNIEWSKI[12]

[1] Department of Earth and Space Science, Graduate School of Science, Osaka University, Osaka, Japan; konishi@iral.ess.sci.osaka-u.ac.jp.
[2] Eureka Scientific, Oakland, CA, USA
[3] Goddard Space Flight Center, Greenbelt, MD, USA
[4] The University of Arizona, Tucson, AZ, USA
[5] Carnegie Institution of Washington, Washington, DC, USA
[6] College of Charleston, Charleston, SC, USA
[7] Space Telescope Science Institute, Baltimore, MD, USA
[8] Max Planck Institute for Astronomy, Heidelberg, Germany
[9] University of Wyoming, Laramie, WY, USA
[10] Jet Propulsion Laboratory, California Institute of Technology, Pasadena CA, USA
[11] University of Tokyo, Tokyo, Japan
[12] University of Oklahoma, Norman, OK, USA

ABSTRACT

We report the discovery of a scattering component around the HD 141569 A circumstellar debris system, interior to the previously known inner ring. The discovered inner disk component, obtained in broadband optical light with *Hubble Space Telescope*/Space Telescope Imaging Spectrograph coronagraphy, was imaged with an inner working angle of $0{.}''25$, and can be traced from $0{.}''4$ (~46 AU) to $1{.}''0$ (~116 AU) after deprojection using $i = 55°$. The inner disk component is seen to forward scatter in a manner similar to the previously known rings, has a pericenter offset of ~6 AU, and break points where the slope of the surface brightness changes. It also has a spiral arm trailing in the same sense as other spiral arms and arcs seen at larger stellocentric distances. The inner disk spatially overlaps with the previously reported warm gas disk seen in thermal emission. We detect no point sources within $2''$ (~232 AU), in particular in the gap between the inner disk component and the inner ring. Our upper limit of $9 \pm 3\,M_J$ is augmented by a new dynamical limit on single planetary mass bodies in the gap between the inner disk component and the inner ring of $1\,M_J$, which is broadly consistent with previous estimates.

Key words: circumstellar matter – stars: imaging – stars: individual (HD 141569 A)

1. INTRODUCTION

There are a number of circumstellar disks associated with young stars that can be characterized as having small dust masses, but still retain gas. Some show localized gas emission (e.g., β Pic; Dent et al. 2014), but others have centrally concentrated gas and millimeter-sized debris (e.g., HD 21997; Kóspál et al. 2013; Moór et al. 2013). There are the disks in which gaps or cavities have formed, possibly in tandem with giant-planet formation. In particular, these systems challenge the practice of inferring the physical properties of the debris disks by modeling the infrared spectral energy distribution (SED).

HD 141569 A is a B9.5 star (Merín et al. 2004) located at 116 ± 8 pc (van Leeuwen 2007) from the Sun, and its age is reported to be 5 ± 3 Myr (Weinberger et al. 2000). A mid-infrared excess detected by the *Infrared Astronomical Satellite* (*IRAS*; Walker & Wolstencroft 1988; Sylvester et al. 1996) suggested that dust exists around HD 141569 A. Disk structures around HD 141569 A were first imaged by Augereau et al. (1999), and Weinberger et al. (1999) discovered two rings using the Near Infrared Camera and Multi-Object Spectrometer (NICMOS) on board *Hubble Space Telescope* (*HST*). The system was subsequently imaged in the optical (Mouillet et al. 2001; Clampin et al. 2003) using the *HST* Space Telescope Imaging Spectrograph (STIS) and Advanced Camera for Surveys (ACS), respectively. The disk has also been imaged using ground-based adaptive optics systems (Boccaletti et al. 2003; Janson et al. 2013; Wahl et al. 2014; Biller et al. 2015; Mazoyer et al. 2016). While complex structures were detected, the coronagraphic studies did not find dust interior to ~175 AU due to analysis technique issues. However, mid-infrared observations detected thermal emission from small particles within $1''$ of the star (Fisher et al. 2000; Marsh et al. 2002). These observations used filters containing strong polycyclic aromatic hydrocarbon (PAH) transitions, so that the nature of the material they detected remained unclear. Gas in the system has been studied in the millimeter (Péricaud et al. 2014), the mid-infrared, and the far-infrared (Thi et al. 2014), with an inner disk component detected from ~13 to ~59 AU (Goto et al. 2006) using its distance of 116 pc. HD 141569 A has two M-type companions (~$8''$, Weinberger et al. 2000) that may produce the outer spirals (Clampin et al. 2003).

Herein we present new imagery of the HD 141569 A circumstellar debris system. The *HST*/STIS imagery has an inner working angle (IWA) of $0{.}''25$. Our observations confirm

---

[*] Based on data collected by the *Hubble Space Telescope*, operated by the Space Telescope Science Institute.
[13] Hubble Fellow.

the previously reported outer disk structures and discover the presence of an inner dust disk component.

2. OBSERVATIONS AND DATA REDUCTION

2.1. Observations

We imaged HD 141569 A and a point-spread function (PSF) reference star (HD 135298, A0V, $B - V = 0.08$)[14] using $HST/$ STIS on 2015 June 12 and 2015 August 18, as part of the general observer program (ID: 13786, PI: G. Schneider). We observed using two coronagraphic image plane masks, WEDGEA1.0 and BAR5 (see Section 12.11 of the STIS Instrument Handbook; Biretta 2015), and observed the PSF reference star interleaved with the HD 141569 observations (Table 1). The WEDGEA1.0 imagery is used, following Schneider et al. (2014), to provide large area deep imaging at the cost of saturation near the coronagraphic wedge. The remaining data are shallower, were obtained using BAR5 ("the bent finger"), fill in the region saturated in the WEDGEA1.0 imagery, and provide an IWA as small as $0.''25$.[15] For the BAR5 observations, we employed three-point dithering (center and ± 0.25 pixel perpendicular to the long axis of the bar) to mitigate the effects of target miscentering and to achieve the smallest possible IWA. Three sets of BAR5 data and one set of WEDGEA1.0 data were obtained per visit. The observations were divided into several sub-exposures per set to facilitate cosmic-ray removal. The total integration time of HD 141569 A is 9.67×10^3 (WEDGEA1.0) and 9.07×10^2 s (BAR5), and that of the PSF reference star is 3.22×10^3 (WEDGEA1.0) and 1.09×10^2 s (BAR5). We used sub-array readouts to reduce overhead times for our many exposures. The field of view (FoV) is 1024 pix $\times$ 427 pix ($52'' \times 22''$) and 1024 pix $\times$ 100 pix ($52'' \times 5.''1$) in WEDGEA1.0 and BAR5, respectively. The data were taken at six spacecraft roll angles (see Table 1, ORIENTAT). As demonstrated in Schneider et al. (2014), combining such data reduces the area obscured by the STIS coronagraphic occulting structure and decorrelates image artifacts that are stable in the instrument.

2.2. Data Reduction

For basic instrumental calibration at the exposure level, we made use of the STIS calibration pipeline *calstis* software (Bostroem & Proffitt 2011) and calibration reference files provided by the Space Telescope Science Institute (STScI). The *calstis* pipeline software performs bias and dark current subtraction, as well as flat-field correction producing "FTL" files in instrumental count units. We median combined *NUMEXP* exposures in each set (4 exposures in WEDGEA1.0 and 8 exposures in BAR5), in order to remove pixels affected by cosmic rays, and then converted the count unit to a count s^{-1} unit by dividing each exposure time (EXPTIME in Table 1).

The stellar PSF was subtracted using the method described in Schneider et al. (2014), using the Interactive Data Language (IDL)-based IDP3 (Image Display Paradigm #3; Stobie & Ferro 2006) software.[16] This step subtracts a scaled and registered version of the reference star HD 135298 from each

HD 141569 A target image. The brightness scaling factor was calculated as 1.067 from the difference of B-magnitudes between the HD 141569 A (7.20) and HD 135298 (7.27) (see footnote 14). We used the B-magnitude in this calculation because the effective wavelength of this bandpass is most representative of a B9.5 star as shown by $HST/$STIS ($\lambda_{\rm eff} \sim$ 4400 Å). The star's position was defined as the crossing point of the diffraction spikes since the star was occulted by the WEDGEA1.0/BAR5 and was not measured directly. In the BAR5 observation, the PSF subtraction was done in all target-to-PSF template dither combinations. We selected the best subtraction in each target image (top six panels in Figure 1). For example, we made nine subtracted images per visit (three dithering target images $\times$ three dithering reference images), and then selected one per dithering (three images in this case) that achieved the smallest IWA. Within each visit, after target-minus-PSF template subtraction of the images in the instrument frame, we rotated the difference images about the occulted star to a common celestial frame. Then, suitable masks were made with IDP3 for each rotated image to occult non-physical features (diffraction spikes, coronagraphic mask structures, saturated pixels) and masking of the binary components HD 141569 BC. All images were registered to a common center and then median combined (bottom three panels in Figure 1). This combination of data from six different spacecraft roll angles removes all hot and dead pixels. In WEDGEA1.0 data, we also used the *cosmicrays* task in Image Reduction and Analysis Facility (IRAF) before PSF subtraction to remove the hot and dead pixels since there were not enough frames at each roll angle to adequately filter them. Finally, the BAR5 image was inserted in the void area of the WEDGEA1.0 image.

We did not use processing techniques for angular differential imaging (e.g., Marois et al. 2006; Lafrenière et al. 2007; Soummer et al. 2012) because they introduce structure distortions (Milli et al. 2012) and the BAR5 imagery has a limited amount of data.

3. RESULTS

3.1. Discovery of an Inner Disk Component

We detect an inner disk component interior to the previously reported rings in all 6 BAR5 observations and the outer extent in WEDGEA1.0 data (Figure 1). In BAR5 data (top panels of Figure 1), the inner signal is elliptical in shape, aligned with the disk major axis (PA = $357°$ from the north), and moves with the sky. This is not the behavior expected from PSF subtraction residuals that are very close to circularly symmetric at low spatial frequencies (Schneider et al. 2014) and intrinsic to the disk due to the system inclination to the line of sight. We therefore conclude that we have discovered an inner component to HD 141569 A's disk. In the bottom right panel of Figure 1, we display the merged BAR5 image with an elliptical line of $i = 55°$ (Mouillet et al. 2001). Figure 2 shows the merged WEDGEA1.0 and BAR5 imagery displayed with a stretch optimized for signal within $4''$ of the star, as well as a cartoon showing our adopted nomenclature for the disk structures. We refer to the outer ring as Component A, the inner ring as Component B, and the newly imaged inner disk component as Component C. We also refer to the gap between Components A and B as Gap AB, and the gap between Components B and C as Gap BC.

---

[14] Taken from SIMBAD, http://simbad.u-strasbg.fr/simbad/.
[15] See "*Hubble Space Telescope* STIS Coronagraphic BARs," http://www.stsci.edu/hst/stis/strategies/pushing/coronagraphic_bars.
[16] https://archive.stsci.edu/prepds/laplace/idp3.html

Table 1
Observation Log

Target Name	UT Date	Visit#	ORIENTAT[a]	CORONAGRAPH	EXPTIME[b]	NUMEXP[c]	TINTTIME[d]	DATASET[e]
HD 141569 A	2015 Jun 12	visit1	111.53	BAR5	6.3	8	50.4	ocjc35010, ocjc35020, ocjc35030
				WEDGEA1.0	400	4	1600	ocjc35040
		visit2	95.53	BAR5	6.3	8	50.4	ocjc36010, ocjc36020, ocjc36030
				WEDGEA1.0	400	4	1600	ocjc36040
		visit4	81.53	BAR5	6.3	8	50.4	ocjc38010, ocjc38020, ocjc38030
				WEDGEA1.0	400	4	1600	ocjc38040
HD 135298	2015 Jun 12	visit3	81.01	BAR5	6.8	8	54.4	ocjc37010, ocjc37020, ocjc37030
				WEDGEA1.0	400	4	1600	ocjc37040
HD 141569 A	2015 Aug 18	visit5	56.53	BAR5	6.3	8	50.4	ocjc31010, ocjc31020, ocjc31030
				WEDGEA1.0	405.7	4	1622.8	ocjc31040
		visit6	46.53	BAR5	6.3	8	50.4	ocjc32010, ocjc32020, ocjc32030
				WEDGEA1.0	405.7	4	1622.8	ocjc32040
		visit8	36.53	BAR5	6.3	8	50.4	ocjc34010, ocjc34020, ocjc34030
				WEDGEA1.0	405.7	4	1622.8	ocjc34040
HD 135298	2015 Aug 18	visit7	58.80	BAR5	6.8	8	54.4	ocjc33010, ocjc33020, ocjc33030
				WEDGEA1.0	405.5	4	1622	ocjc33040

Notes.

[a] Position angle of the image $+Y$ axis measured eastward from celestial north (degree).

[b] Individual exposure times (s).

[c] Number of exposures.

[d] Total integration time (s); EXPTIME $\times$ NUMEXP.

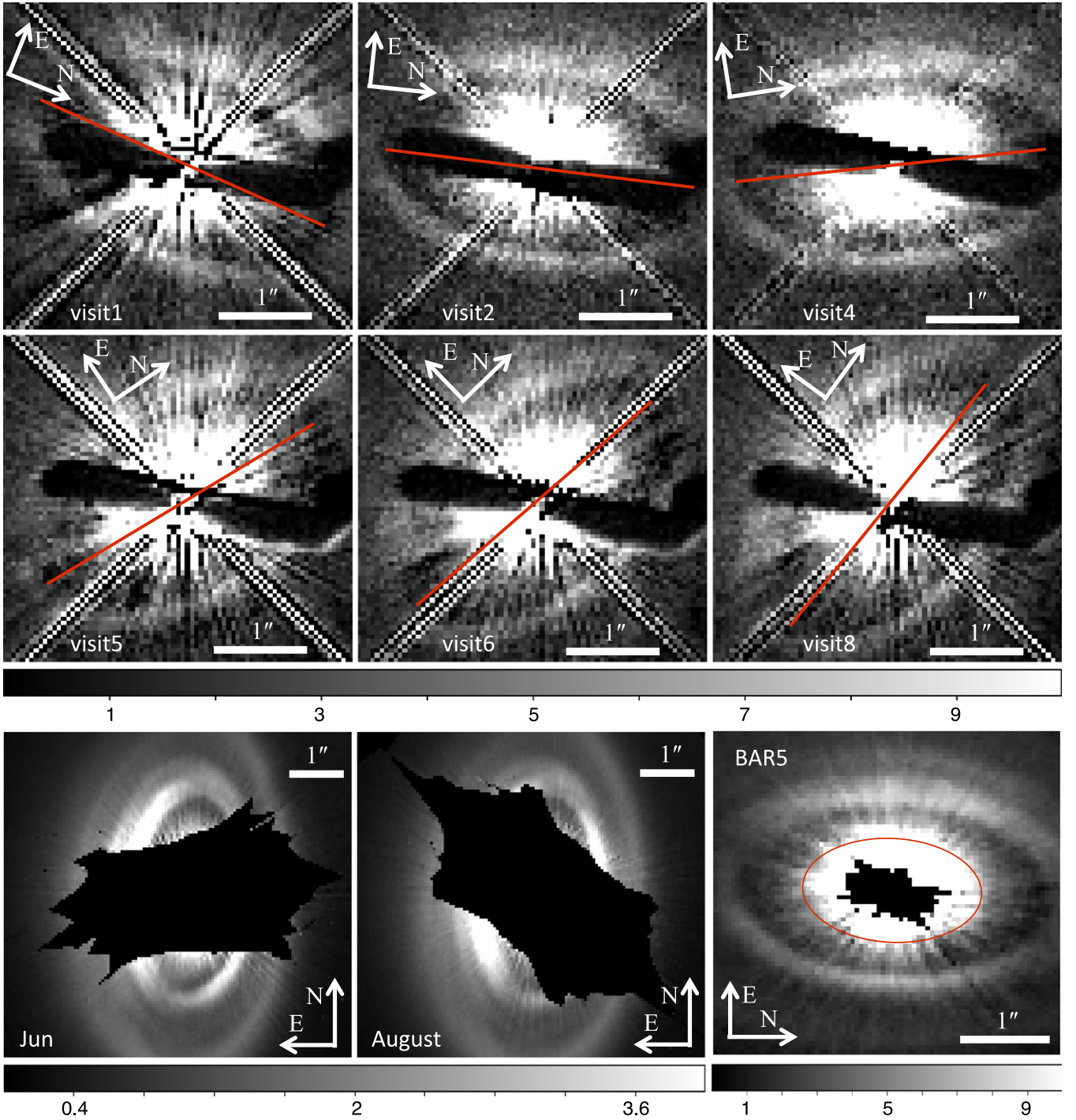[e] Same as ROOTNAME in the header and fits file name.

Figure 1. Top six panels: PSF-template-subtracted images of HD 141569 circumstellar disk at six separate field orientations using the BAR5 mask revealing the inner dusk component (Component C), and inner ring component (Component B). Red lines show the major axis of Component B. See Table 1 for details. Bottom left two panels: deep imaging with the WEDGEA1.0 mask obscures most of Component C imaged with BAR5, but cleanly images the rings (Components A and B) beyond, as shown separately at the two observational epochs designed to provide maximum visibility around the star. Bottom right panel: the merged BAR5 image with a red line represents a disk at $i = 55°$ and PA = 357°. The scale unit is count s^{-1}.

Component C has no flux drop down to 0″.25 and an outer radial extent of 1″.0 defined from breaks seen in the radial surface brightness (SB) profile (see Section 3.3 for more details). The fit of the bottom right panel of Figure 1 follows Component C and suggests it is also at $i = 55°$. We therefore use this specific angle to deproject the disk. In the surface density (SD) view, Component C has a spiral arm at 1″.1 (see Section 3.3).

Figure 2(a) shows a final composite image, with both the data void and M-type companions masked as black. Figure 2(a) reproduces the previously reported azimuthal brightness asymmetries in Components A and B (Weinberger et al. 1999; Mouillet et al. 2001; Clampin et al. 2003) and suggests that these extend into Component C. For further measurement and analysis, we deprojected the system using inclination $i = 55°$ to make Figure 2(b), and then follow the Clampin et al.
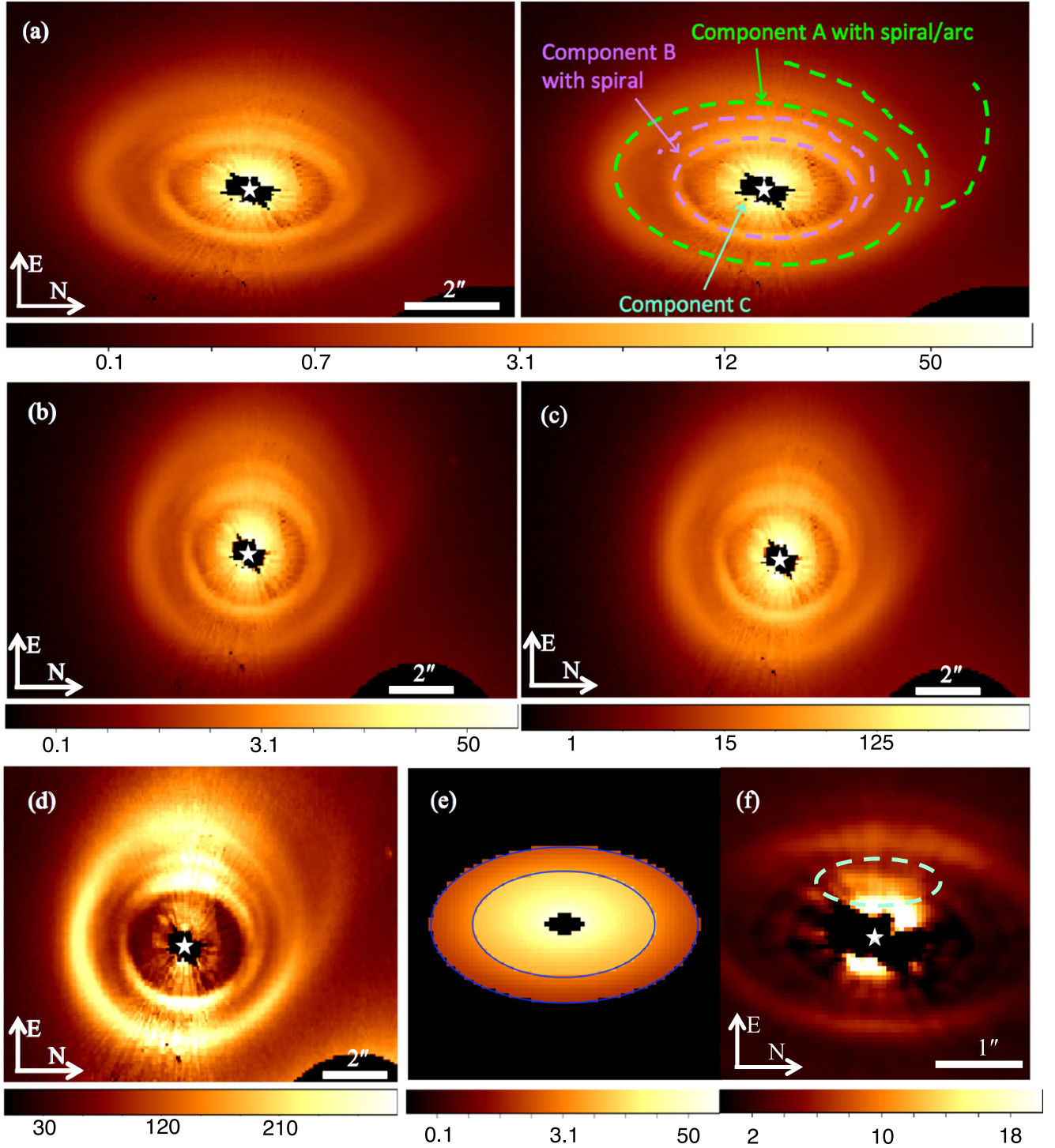
Figure 2. (a) Final image. In the right image, our nomenclature is annotated on the same image as presented at left. (b) Deprojected image assuming $i = 55°$. (c) Deprojected and phase-corrected image using $g = 0.1$. (d) Deprojected and phase-corrected image multiplied by r^2, which is a proxy to a surface density map. Star marks are the primary star's position. The central obscuration and binary stars at bottom right are masked as black. (e) Toy disk model made in Section 3.3. Blue ellipses are boundary of model disks. (f) Composite BAR5 image subtracted a toy disk. The color scale is lognormal in (a), (b), (c), and (e) and linear in (d) and (f). The scale unit is count s^{-1}.

(2003) methodology to correct the phase function and illumination effects. After deprojection (Figure 2(b)), the stellocentric mask-limited IWA of our data is 0″4 (~46 AU).

3.2. Grain Forward Scattering

We found a similar brightness asymmetry between the east and west for Component C along the disk minor axis (see Figure 2(a)) as previously reported for Components A and B in the visible and near-infrared (Weinberger et al. 1999; Mouillet et al. 2001; Clampin et al. 2003). The radial SB of the east side between 0″7 and 1″0 is 2.0 ± 0.1 × brighter than that of the west side (the SB calculation is described in Section 3.3). This is similar to the measured asymmetry in Mouillet et al. (2001) and slightly larger than Weinberger et al. (1999) at 1.1 μm.

This asymmetric ratio corresponds to $g = 0.14$–0.15 in the Henyey–Greenstein phase function (Henyey & Greenstein 1941) assuming a geometrically thin disk and $i = 55°$. Clampin et al. (2003) reported that Components A and B are not azimuthally uniform. We adjusted g values assuming that this non-uniform SB feature is continued in Component C and obtained a best-fit value with $g = 0.1$. This is consistent with the result of Weinberger et al. (1999) and Mouillet et al. (2001). We note that our g value is a lower limit because the degree of forward scattering for debris disks is underestimated (Hedman & Stark 2015). This problem was addressed in Stark et al. (2014). Figure 2(c) shows the image after correcting for the scattering phase function asymmetry.

3.3. Radial Surface Density and Brightness Profile

We multiplied Figure 2(c) by r^2 (arcsec^2) to correct for the radial illumination, which provides a proxy SD map (see Figure 2(d)). In order to investigate detailed structures, the SB and SD profiles were made (Figure 3) using the deprojected image and the SD image (Figures 2(b) and (d)). We calculated the mean within each small section (radial: 2 pixels, azimuth: 5°) and converted counts s^{-1} pixel^{-1} to flux density F_λ (erg cm^{-2} s^{-1} Å^{-1} pixel^{-1}) according to the equation described in Section 5.3 of Bostroem & Proffitt (2011), and errors on these measurements were calculated as the 1σ scatter within a section. The SD profile in Figure 3 was normalized by the south peak of Component B (5.0×10^{-17} erg arcsec^2 cm^{-2} s^{-1} Å^{-1}). We note again that STIS has a broad bandpass and cannot specify a single wavelength. For STIS, 1 count s^{-1} is 4.55×10^{-7} Jy according to Schneider et al. (2014) and one square arcsec is approximately 388 pixels.

The SB of Component C has slope breaks, which are points where the SB drops, along the major axis at $\sim 1''$. The location of the breaks is $1''0$ (~ 116 AU) in the north and $0''9$ (~ 104 AU) in the south. The difference between the north and south breaks indicate that the Component C center is offset of $0''05$ (~ 6 AU) toward the north. There is no clear break in the east and west side probably due to an elongation effect introduced by the deprojection. We place no tight constraint on the Component C center along the minor axis, but note that Gap BC is slightly shifted to east according to SB in Figure 3. It might be caused by a pericenter offset of Component C. A spiral arm could be detected at $1''1$ (~ 128 AU) in the east side seen in Figure 2(d) and SD profile in Figure 3, with same sense as the outer spirals.

We made a toy disk model (Figure 2(e)) using SB indices, and subtracted it from the composite BAR5 image. The SB has two components inside Component B, and thus the toy disk has a -1.4 index from $0''25$ to $1''0$ (Component C) and a -3.0 index from $1''0$ to $1''4$ (halo between Component B and C). We also assumed $i = 55°$, $g = 0.1$, and PA = 357°, and pericenter offset of 1 pixel (~ 6 AU) toward north when made and subtracted it. Figure 2(f) shows the 3×3-box smoothed image. It has boundaries due to edges of the toy disk, but we detect brighter residuals in the east side extended at Component C (enclosed area by a cyan line). These residuals may have a spiral arc-like geometry similar to other arcs in this system.

3.4. Sensitivity to Exoplanets

We detected no point sources within $2''$ (~ 232 AU) of the star in the PSF-template-subtracted image. We calculated the sensitivity to exoplanets that may exist within the disk and report our detection limits (see Brandt et al. 2013). The 1σ noise was calculated from the standard deviation of SB profile (employed same calculation as Section 3.3) assuming that only the core of the PSF (1 pixel) can be detected. Figure 4 shows the 5σ ($5 \times 1\sigma$) contrast curve, which we consider the sensitivity limit of the observations. To calculate a contrast relative to the primary, the primary star count rate for our observation was estimated using the STIS imaging ETC[17] since it was occulted by wedge structures. We used a template A0-type spectrum and normalized it using the V magnitude of HD 141569 A. Then the 5σ noise was divided by the estimated primary star's count rate (2.1×10^6 count s^{-1}). We confirmed the contrast is reasonable by embedding some artificial stars.

Exoplanetary mass estimates are shown in the right side of Figure 4. They were estimated from the BT-Settl evolutionary model (Allard et al. 2011). We took the spectra of sub-stellar objects (20, 15, 10, 8, and 5 M_J at 5 Myr) from the Phoenix web simulator[18] and calculated each count rate that would be obtained in our observation, using the STIS imaging ETC.

In Gap BC, which is considered to be formed by a giant planet, the PSF core of the possible planet is from 0.5 to 4.5 counts s^{-1}. It corresponds to the contrast of point sources from 2.1×10^{-6} down to 2.4×10^{-7} in Gap BC. Converted to mass, our luminosity upper limit corresponds to a mass upper limit of 9 ± 3 M_J.

4. DISCUSSION

4.1. Inner Disk Component

Compared with previous STIS and ACS imagery, Mouillet et al. (2001) and Clampin et al. (2003) did not recover Component C due to the occultation. The IWA of ground-based observations have reached $0''3$ (Biller et al. 2015), but the sensitivity to faint structures at this IWA are more difficult to recover with their processing because it caused significant self-subtraction at small IWA.

Our imaged Component C overlaps partially with the disk seen in mid-infrared thermal emission (Fisher et al. 2000; Marsh 2002). A warm disk in CO emission was detected by Goto et al. (2006) at 13–59 AU based on a more recent stellar parallax from van Leeuwen (2007). The Component C material we now see in scattered light is, in part, in the same stellocentric region as the CO emission. A spatial overlap of especially small-grain dust and gas is expected in a transitional disk. HD 141569 A disk has some transitional disk characteristics, which might indicate that this system is in an evolutionary stage between transitional and debris disks. Our Component C traces dust beyond the radius reported by T. Currie et al. (2016, in preparation) and partially overlaps with the warm CO disk reported by Goto et al. (2006) and the PAH disk reported by Thi et al. (2014). Small dust grains such as we view in the broadband optical are expected to be coupled to the gas (Takeuchi & Artymowicz 2001). This prediction can be confirmed with the ALMA data (see T. Currie et al. 2016, in preparation).

---

[17] http://etc.stsci.edu/etc/input/stis/imaging/
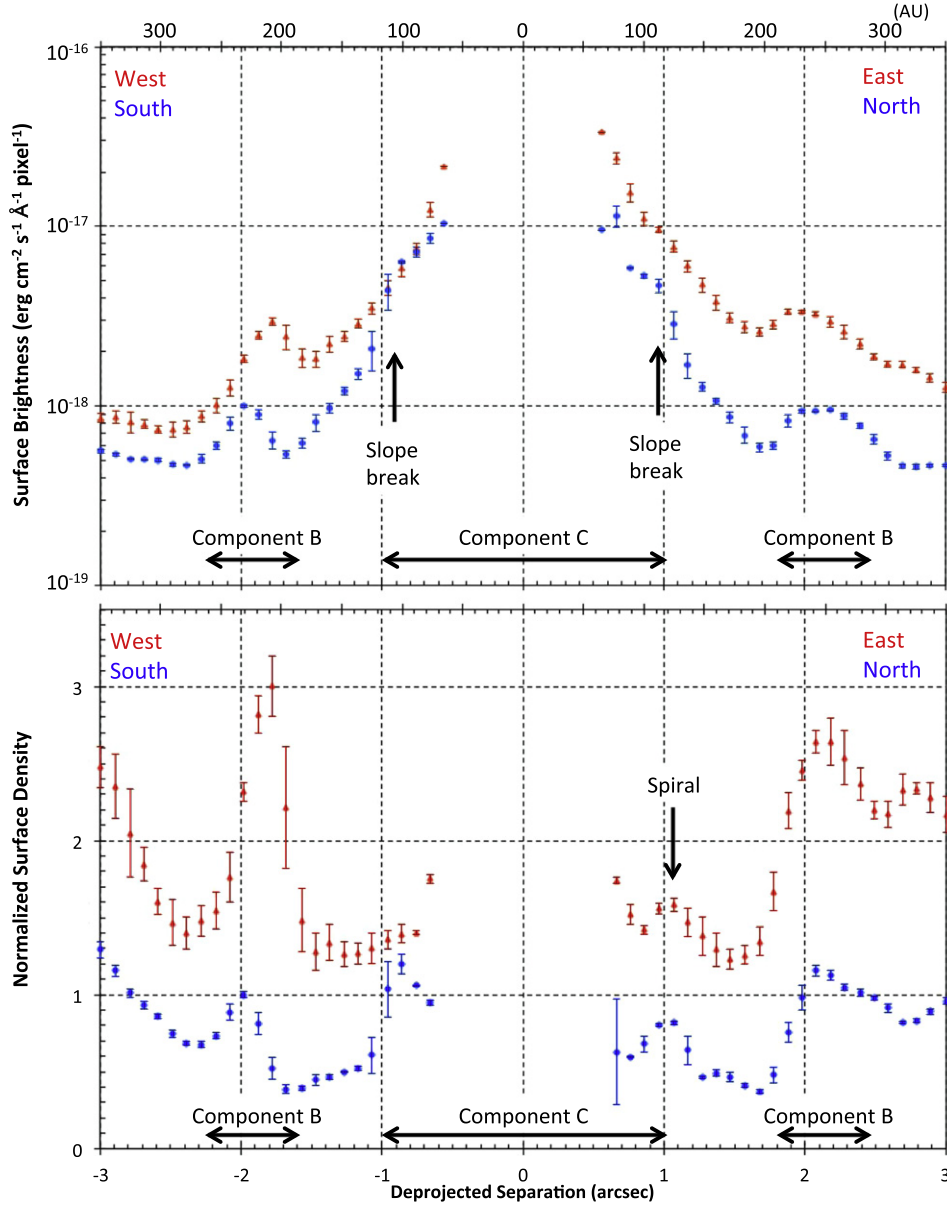[18] https://phoenix.ens-lyon.fr/simulator/index.faces

Figure 3. Top panel: surface brightness (SB) profile along the major (N/S) and minor (E/W) axis of Figure 2(b). Bottom panel: normalized surface density (SD) profile along the major and minor axis of Figure 2(d). Plotted here is the normalized SD profile after correcting for a phase function assuming a $g = 0.1$ asymmetry parameter with $i = 55°$. For normalization, the peak value south of Component B was used.

4.2. Dynamical Limits on Planets

Wisdom (1980) used the resonance overlap criterion to analytically derive the relationship between the width of a gap and the mass of the planet in a collisionless disk. Nesvold & Kuchner (2015) used numerical simulations of a collisional disk to estimate a time-dependent gap law. This collisional gap law is based on gas-free N-body simulations of a planetesimal belt and does not consider the effects of gas drag or radiation pressure on dust dynamics, all of which may be important in the case of HD 141569. However, Ardila et al. (2005) simulated the effects of both gas drag and radiative forces on the dust in HD 141569 A. Therein they found that their simulated planetesimal distribution resembled the observed dust distribution. The gap law can be used to place upper limits on the mass of a planet orbiting in a gap, but it is limited by a degeneracy between the planet mass and the radial distance between the planet and the gap. Because we measure the location of both the inner and outer edge of the gap in the HD 141569 A disk, we can break this degeneracy by assuming that the gap contains a planet on a circular orbit at the midpoint between the gap edges (137.5 AU for Gap BC). Assuming a system age of 5 Myr and stellar mass of 2.5 $M_{\odot}$ (Weinberger et al. 2000), and estimating the vertical optical depth of the disk as $L_{IR}/L_{star} = 1.8 \times 10^{-2}$ (Merín et al. 2004), we use the technique of Nesvold & Kuchner (2015) to place an upper limit of 1 M_J on a hypothetical planet orbiting in Gap BC.

Because we detect a hot dust population close to the star, we are able to constrain the size of Gap BC and therefore our upper limit for the planet in Gap BC, 1 M_J, is smaller than those of Ardila et al. (2005) and Reche et al. (2009). Further numerical simulations are needed to determine the best-fit system architecture to explain the dust distribution in the disk.
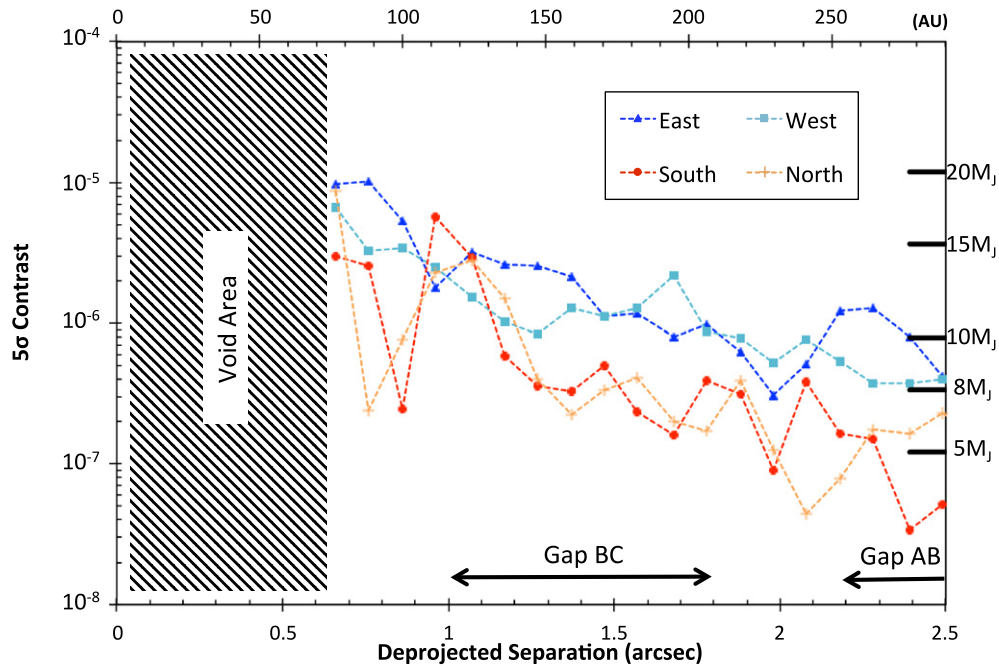
Figure 4. 5σ detection limits on exoplanets. The abscissa and ordinate axes are deprojected separation and 5σ contrast relative to the primary star, respectively. The shaded area is occulted by the wedge. The right ordinate axis shows the corresponding mass estimated from the star evolution model (BT-Settl). More details are given in Section 3.4.

5. SUMMARY

We detected an inner disk component around HD 141569 A with *HST*/STIS in the optical. The disk component is traced from 0″4 (∼46 AU) to 1″0 (∼116 AU) after deprojection using $i = 55°$. It has SB radial profile breaks, a pericenter offset of 6 AU, and a spiral arm at 1″1 and overlaps partially with the previously known warm CO disk.

REFERENCES

Allard, F., Homeier, D., & Freytag, B. 2011, in ASP Conf. Ser. 448, 16th Cambridge Workshop on Cool Stars, Stellar Systems, and the Sun, ed. C. Johns-Krull, M. K. Browning, & A. A. West (San Francisco, CA: ASP), 91
Ardila, D. R., Lubow, S. H., Golimowski, D. A., et al. 2005, ApJ, 627, 986
Biller, B. A., Liu, M. C., Rice, K., et al. 2015, MNRAS, 450, 4446
Biretta, J. 2015, STIS Instrument Handbook Version 14.0 (Baltimore, MD: STScI)
Boccaletti, A., Augereau, J.-C., Marchis, F., & Hahn, J. 2003, ApJ, 585, 494
Bostroem, K. A., & Proffitt, C. 2011, STIS Data Handbook v. 6.0
Brandt, T. D., McElwain, M. W., Turner, E. L., et al. 2013, ApJ, 764, 183
Clampin, M., Krist, J. E., Ardila, D. R., et al. 2003, AJ, 126, 385
Dent, W. R. F., Wyatt, M. C., Roberge, A., et al. 2014, Sci, 343, 1490
Fisher, R. S., Telesco, C. M., Piña, R. K., Knacke, R. F., & Wyatt, M. C. 2000, ApJL, 532, L141
Goto, M., Usuda, T., Dullemond, C. P., et al. 2006, ApJ, 652, 758
Hedman, M. M., & Stark, C. C. 2015, ApJ, 811, 67
Henyey, L. G., & Greenstein, J. L. 1941, ApJ, 93, 70
Janson, M., Brandt, T. D., Moro-Martín, A., et al. 2013, ApJ, 773, 73
Kóspál, Á, Moór, A., Juhász, A., et al. 2013, ApJ, 776, 77
Lafrenière, D., Marois, C., Doyon, R., Nadeau, D., & Artigau, É 2007, ApJ, 660, 770
Marois, C., Lafrenière, D., Doyon, R., Macintosh, B., & Nadeau, D. 2006, ApJ, 641, 556
Marsh, K. A., Silverstone, M. D., Becklin, E. E., et al. 2002, ApJ, 573, 425
Mazoyer, J., Boccaletti, A., Choquet, E., et al. 2016, ApJ, in press (arXiv:1601.00505)
Merín, B., Montesinos, B., Eiroa, C., et al. 2004, A&A, 419, 301
Milli, J., Mouillet, D., Lagrange, A.-M., et al. 2012, A&A, 545, A111
Moór, A., Juhász, A., Kóspál, Á, et al. 2013, ApJL, 777, L25
Mouillet, D., Lagrange, A. M., Augereau, J. C., & Ménard, F. 2001, A&A, 372, L61
Nesvold, E. R., & Kuchner, M. J. 2015, ApJ, 798, 83
Péricaud, J., Di Folco, E., Dutrey, A., et al. 2014, in Thirty years of Beta Pic and Debris Disks Studies, ed. A.-M. Langrange & A. Boccaletti (Paris: Institut d'Astrophysique de Paris), 58
Reche, R., Beust, H., & Augereau, J.-C. 2009, A&A, 493, 661
Schneider, G., Grady, C. A., Hines, D. C., et al. 2014, AJ, 148, 59
Soummer, R., Pueyo, L., & Larkin, J. 2012, ApJL, 755, L28
Stark, C. C., Schneider, G., Weinberger, A. J., et al. 2014, ApJ, 789, 58
Stobie, E., & Ferro, A. 2006, in ASP Conf. Ser. 351, Astronomical Data Analysis Software and Systems XV, ed. C. Gabriel et al. (ASP: San Francisco, CA), 540
Sylvester, R. J., Skinner, C. J., Barlow, M. J., & Mannings, V. 1996, MNRAS, 279, 915
Takeuchi, T., & Artymowicz, P. 2001, ApJ, 557, 990
Thi, W.-F., Pinte, C., Pantin, E., et al. 2014, A&A, 561, A50
van Leeuwen, F. 2007, A&A, 474, 653
Wahl, M., Metchev, S., Patel, R., et al. 2014, in Proc. IAU Symp. 299, ed. M. Booth, B. C. Matthews, & J. R. Graham (Cambridge: Cambridge Univ. Press), 72
Walker, H. J., & Wolstencroft, R. D. 1988, PASP, 100, 1509
Weinberger, A. J., Becklin, E. E., Schneider, G., et al. 1999, ApJL, 525, L53
Weinberger, A. J., Rich, R. M., Becklin, E. E., Zuckerman, B., & Matthews, K. 2000, ApJ, 544, 937
Wisdom, J. 1980, AJ, 85, 1122